Tectonophysics 850 (2023) 229752

Contents lists available at ScienceDirect

Tectonophysics

journal homepage: www.elsevier.com/locate/tecto

The effect of along-strike variable plate deflection on bending stress and seismicity at the southern Mariana Trench

Jiangyang Zhang [a,b,c], Hongfeng Yang [c,d,*], Gaohua Zhu [e], Han Chen [d], Fan Zhang [a,b], Zhen Sun [a,b]

[a] Key Laboratory of Ocean and Marginal Sea Geology, South China Sea Institute of Oceanology, Chinese Academy of Sciences, Guangzhou 510301, China
[b] Southern Marine Science and Engineering Guangdong Laboratory (Guangzhou), Guangzhou 511458, China
[c] Shenzhen Research Institute, The Chinese University of Hong Kong, Shenzhen, 518057, China
[d] Earth and Environmental Sciences Programme, Faculty of Science, The Chinese University of Hong Kong, China
[e] CAS Key Laboratory of Marine Geology and Environment, Institute of Oceanology, Chinese Academy of Sciences, Qingdao 266071, China

ARTICLE INFO

Keywords:
Mariana Subduction zone
Plate bending
Numerical simulation
Stress
Earthquakes

ABSTRACT

Bending-induced faults are often recognized as sources of extensional or compressional earthquakes in the outer rise region, and have been extensively investigated in 2-D plate flexural models. However, such 2D models have difficulty in explaining observed earthquakes caused by reactivation of pre-exsiting fabrics inherited from mid-ridge, especially when the fabrics is oblique to the subduction. Here, we develop a 3-D flexural model to investigate the plate deflection at the southernmost Mariana subduction zone. The Particle Swarm Optimization (PSO) method was used to invert flexural parameters of the subducting plate. It shows that the boundary loading near the Challenger Deep is nearly twice that in the region further east. Under this deformation, the bending stresses within the outer rise vary significantly along the strike of the subduction zone. We find that the location of abrupt stress changes coincides with the outer rise earthquakes which were considered to be reactivation of remnant faults. We proposed a model to illustrate the influence of along-strike variation of plate deflection on bending stress and outer rise earthquakes: The variation of plate deflection along the trench may cause the change of the direction of the maximum extensional bending stress in the variable zone which provides greater possibilities for reactivation of preexisting weak faults, resulting in unevenly distributed outer rise earthquakes, reactivation of remnant fabric or earthquake.

1. Introduction

Widely distributed subduction zone earthquakes may trigger large tsunami and cause significant loss of life and damage (e.g. Gusman et al., 2009; Lay et al., 2010). In addition to interplate earthquakes, intra-plate earthquakes can also be devastating, as seen by the 1977 Sumba Indonesia (Sunda trench, $M_w = 8.3$) (Lynnes and Lay, 1988), the 1990 Mariana Trench ($M_w = 7.3$) (Yoshida et al., 1992), the 2007 Kuril Trench ($M_w = 8.1$) (Ammon et al., 2008), and the 2009 Somoa-Tonga ($M_w = 8.1$) (Beavan et al., 2010; Lay et al., 2010) earthquakes. All of these earthquakes occurred in the outer rise region seaward of the trench, where normal faults are generated or reactivated by plate bending (Mortera-Gutiérrez et al., 2003; Ranero et al., 2003, 2005). There are also large strike-slip earthquakes within outer rise, such as the 1987 Mw 7.9 northeastern Gulf of Alaska earthquakes (Pegler and Das, 1996), the 2012 Sumatra great earthquakes (Mw = 8.6 and 8.2) (Duputel et al., 2012) and the 2018 Mw 7.9 Gulf of Alaska Earthquake (Lay et al., 2018). These strike-slip events apparently do not match with normal faults and require laterally varying plate boundary conditions (Lay et al., 2018). Therefore, evaluating plate bending, stress distribution, and corresponding earthquakes in the outer rise region are crucial to assess earthquake and tsunami hazard in subduction zones.

Previous studies have recognized that the accumulation of bending stress may induce earthquakes (Chapple and Forsyth, 1979; Christensen and Ruff, 1983, 1988; Scholz and Campos, 1995; Bilham et al., 2003; Emry et al., 2014; Zhou et al., 2015; Zhang et al., 2018a, 2018b). For instance, Chapple and Forsyth (1979) explained the depths of extensional and compressional outer rise earthquakes assuming that plate bending can produce tensional and compressional stress regimes, which are separated by a neutral plane. This model was supported by focal

* Corresponding author at: Shenzhen Research Institute, The Chinese University of Hong Kong, Shenzhen, 518057, China.
E-mail address: hyang@cuhk.edu.hk (H. Yang).

https://doi.org/10.1016/j.tecto.2023.229752
Received 14 July 2022; Received in revised form 19 January 2023; Accepted 28 January 2023
Available online 10 February 2023

mechanism solutions of outer rise earthquakes, e.g. along the Mariana subduction zone where the focal depths of normal and thrust faulting events delineate the tension-compression boundary (Emry et al., 2014). Zhang et al. (2014) simulated the geometry of the subducting plate along profiles perpendicular to the Mariana Trench using a two-segment effective elastic thickness (T_e) flexural model. They suggested that the plate bending stresses could exceed the lithosphere yield strength envelope and thus result in faulting and extensional earthquakes in the upper plate, corresponding to the reduction in T_e. Tomographic results of SV-wave velocity structure near the Southern Mariana Trench also supported such extensional faulting and consequent hydration within the incoming plate, as evidenced by distinct low velocities (3.6–4.1 km/s) within the upper ~25 km of the mantle in the subducting plate (Zhu et al., 2021).

The above 2-D flexural models only consider the bending from the direction perpendicular to the trench and imply that the flexural parameters (including axial bending moment (M_0), vertical shear loading (V_0), and in-plane stress) do not change along the trench. However, along-strike variation in both faulting types and depths of outer rise seismicity has been shown in the northern and southern Mariana subduction zone (Emry et al., 2014). More importantly, a new study shows that at the southern Mariana, the depth of outer rise earthquakes can reach nearly 50 km which were considered to be caused by reactivation of the inherited seafloor fabrics (Chen et al., 2022). What is the mechanism of reactivating such deep intraplate faults? Moreover, observations of reactivated faults in outer rise further indicate complex stress fields and thus require investigations considering laterally varying boundary conditions and loadings (Emry et al., 2014), instead of 2-D flexural models.

Some 3-D flexural models have been developed to investigate the subducted plate geometry (Manríquez et al., 2014) and boundary loading variation (Zhang et al., 2018b; Zhang et al., 2019). However, no models have provided constraints on the bending stress. Here we develop a 3-D model by incorporating bathymetries of the incoming plate, geometries of the subducting slab, and M_0 and V_0. We then apply this model in the southern Mariana subduction (Fig. 1) zone and derive bending stress distribution within the incoming plate. The distribution of bending stress is compared to the earthquake locations that were obtained from the recently acquired near-field seismic data (Zhu et al., 2019; Chen et al., 2022). In addition, we discuss the possible relationship between the plate bending, stress, and the distribution of outer rise earthquakes.

2. Data and method

2.1. Data Preparation

Three datasets are used in this study, including 15 arc-second resolution global bathymetry data (Tozer et al., 2019) and local multibeam data with ~150 m resolution (https://www.ngdc.noaa.gov/maps/autogrid/), global slab geometry data (Slab 2.0 from Hayes, 2018), and newly acquired ocean bottom seismic data (Zhu et al., 2019). Firstly, we identify the strikes of the bending-related normal faults (Fig. 2a) from the multibeam data, as did in Ranero et al. (2005) for the Mid-America and the Chile Trench. Fault strike is not necessarily parallel to the bending axis, such as the case when abyssal hill fabric is reactivated (Masson, 1991). The relic spreading-parallel direction is ~20–30°from the fault strike (Fig. 2b), indicating that these faults are generated by bending and thus reflect the bending direction. In order to select the plate boundary parallel to the fault strikes, the model area is chosen following the bending direction (red rectangle in the Fig. 1).

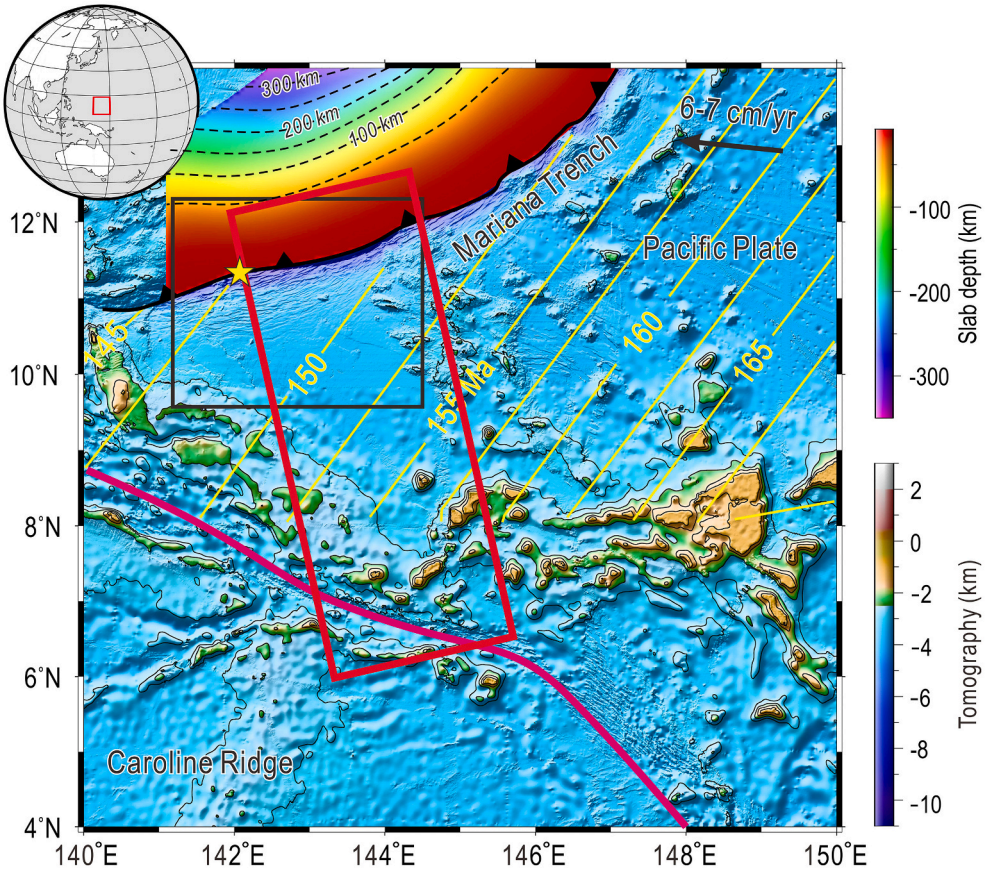

Fig. 1. Seafloor bathymetry of the southern Mariana Trench. The red rectangle is the domain of our 3-D flexural model; the black square box is the area where the normal faults are identified with the multi-beam data (please see Fig. 2a) and the yellow star represents the location of the Challenger Deep. Yellow lines are the magnetic lineation based on Zhou et al. (2015). (For interpretation of the references to colour in this figure legend, the reader is referred to the web version of this article.)

2.2. Flexure model and inversion

Considering the flexure of the subducted plate, the plate is assumed as an elastic layer on an inviscid layer. As such, the flexure deformation of the elastic layer can be modeled by an elastic thin plate under applied external forces (Fig. 3) (Watts, 2001; Turcotte and Schubert, 2014). If the plate bending stress exceeds the lithospheric yield strength, normal faults are generated and may lead to earthquakes in the outer rise (Grevemeyer et al., 2005; Ranero et al., 2005). This process may result in the loss of strength and flexural rigidity of the lithosphere (Contreras-Reyes and Osses, 2010). Therefore, a flexural model with variable flexural rigidity has often been used to model the deformation of the subducted plate (Zhang et al., 2014; Hunter and Watts, 2016; Zhang et al., 2018b).

According to the Kirchhoff-Love of thin plate (Timoshenko and Woinowsky-Krieger, 1959), the governing equation about 3-D plate deflection w(x, y) can then be simplified to 2-D form:

$$\nabla^2\left(D\nabla^2 w\right)-(1-\nu)\times\left(\frac{\partial^2 D}{\partial x^2}\frac{\partial^2 w}{\partial y^2}-2\frac{\partial^2 D}{\partial x\partial y}\frac{\partial^2 w}{\partial x\partial y}+\frac{\partial^2 D}{\partial y^2}\frac{\partial^2 w}{\partial^2 x^2}\right)+\Delta\rho g w=q(x,y) \tag{1}$$

where $\Delta\rho$ is the density contrast between the mantle (ρ_m) and water (ρ_w), $q(x, y)$ is a spatially varying vertical surface loading, and D is the flexural rigidity defined as: $D=\frac{ET_e^3(x,y)}{12(1-\nu^2)}$. Here E is Young's modulus and ν is Poisson's ratio. Generally, E and ν are constant which are set to be 7×10^{10} Pa and 0.25, respectively, but T_e is allowed to vary spatially in our model. Unlike 2-D model in which the boundary bending moment (M_0) and vertical shear stress (V_0) have simple forms, M_0 and V_0 in our model are vectors (All parameters are displayed in the Table 1).

The eq. (1) was solved by the finite-difference method (FDM) under different boundary loadings or surface loading (q(x, y)). The boundary conditions are given by (Fig. 3):

$$\begin{aligned}&\Gamma_1: M=M_0(y), V=V_0(y),\\ &\Gamma_2: M=0, V=0,\\ &\Gamma_3: w=0, M=0,\\ &\Gamma_4: M=0, V=0,\end{aligned} \tag{2}$$

Eq. (2) shows that Γ_1 is the subducting border, Γ_2 and Γ_4 are free borders relative to the deflection w and Γ_3 is the fixed border. We have compared our model with different previous 2-D or 3-D models and the validity and accuracy of our 3-D model have been demonstrated in detail (Zhang et al., 2018b).

Unlike elasto-plastic model (Zhou and Lin, 2018) which simulated faults pattern by plastic strain concentration, our model regards the inelastic deformation of plate (such as the brittle deformation in the upper extensional part) as the reduction in effective elastic thickness (T_e). Zhou and Lin (2018) indicated that the reduction in elastic core modeled by pure elastic model (Zhang et al., 2014) was little greater than that of elasto-plastic model, while the extensional yield depth (d_y) modeled by two models are very close. T_e reduction in our model reflects the inelastic deformation part caused by normal faulting.

Unlike 2-D models, M_0 and V_0 now become vectors rather than scalars, and T_e becomes a matrix rather than a vector (Fig. 3). For simplicity, the T_e is divided into two parts (T_e^M and T_e^m), similar to

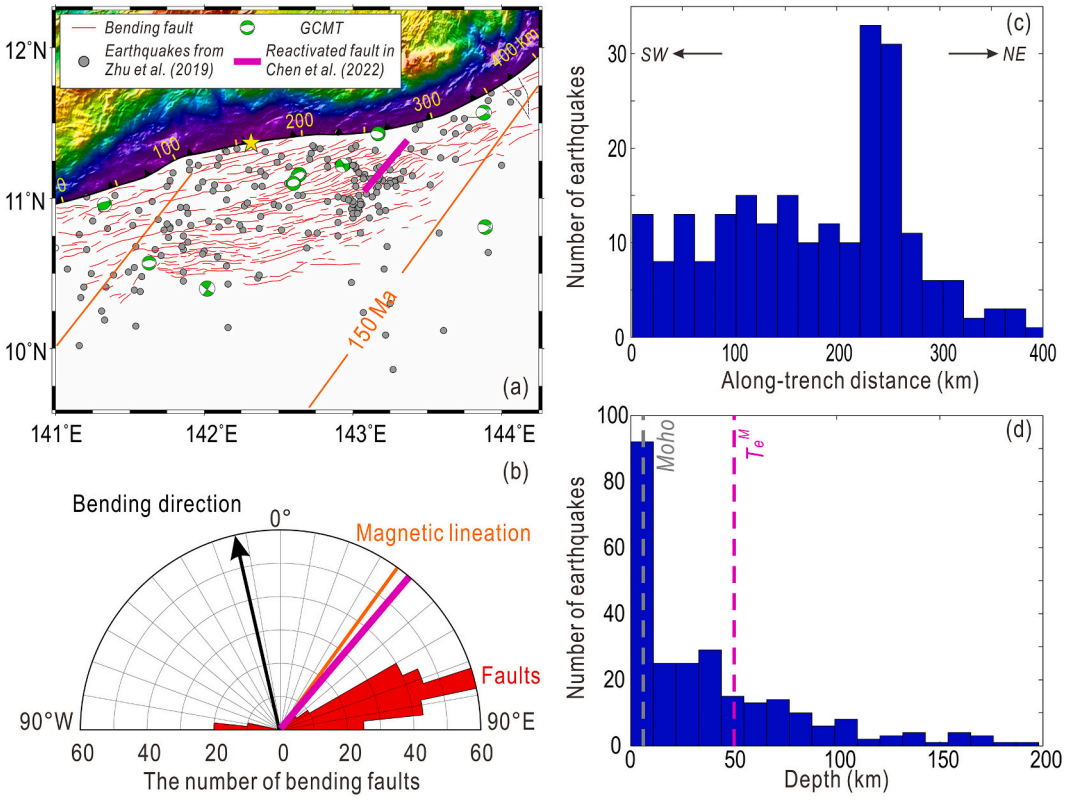

Fig. 2. Statistics of fault strike and seismicity at outer rise. (a) Tectonic structure of the oceanic plate. Red lines are normal faults identified from the multibeam. Orange lines are the magnetic lineation based on Zhou et al. (2015). Grey circles represent locations of earthquakes from Zhu et al. (2019) and focal mechanisms are from GCMT. (b) The rose diagram (red part) shows that the direction of strike of the bending-normal faults is ~N80°E at the southern Marina Trench and the black arrow perpendicular to the fault strike shows that the bending direction is ~N10°W. Orange line suggests that the direction of the magnetic lineation is ~N38°E. (c) Histogram of outer rise earthquakes (within the distance 200 km away the trench) along the strike of trench. (d) Histogram of depth of outer rise earthquakes. It shows that ~25% of earthquakes occur within the depth shallower than 6 km and ~ 75% of earthquakes occur within the depth shallower than 50 km. (For interpretation of the references to colour in this figure legend, the reader is referred to the web version of this article.)

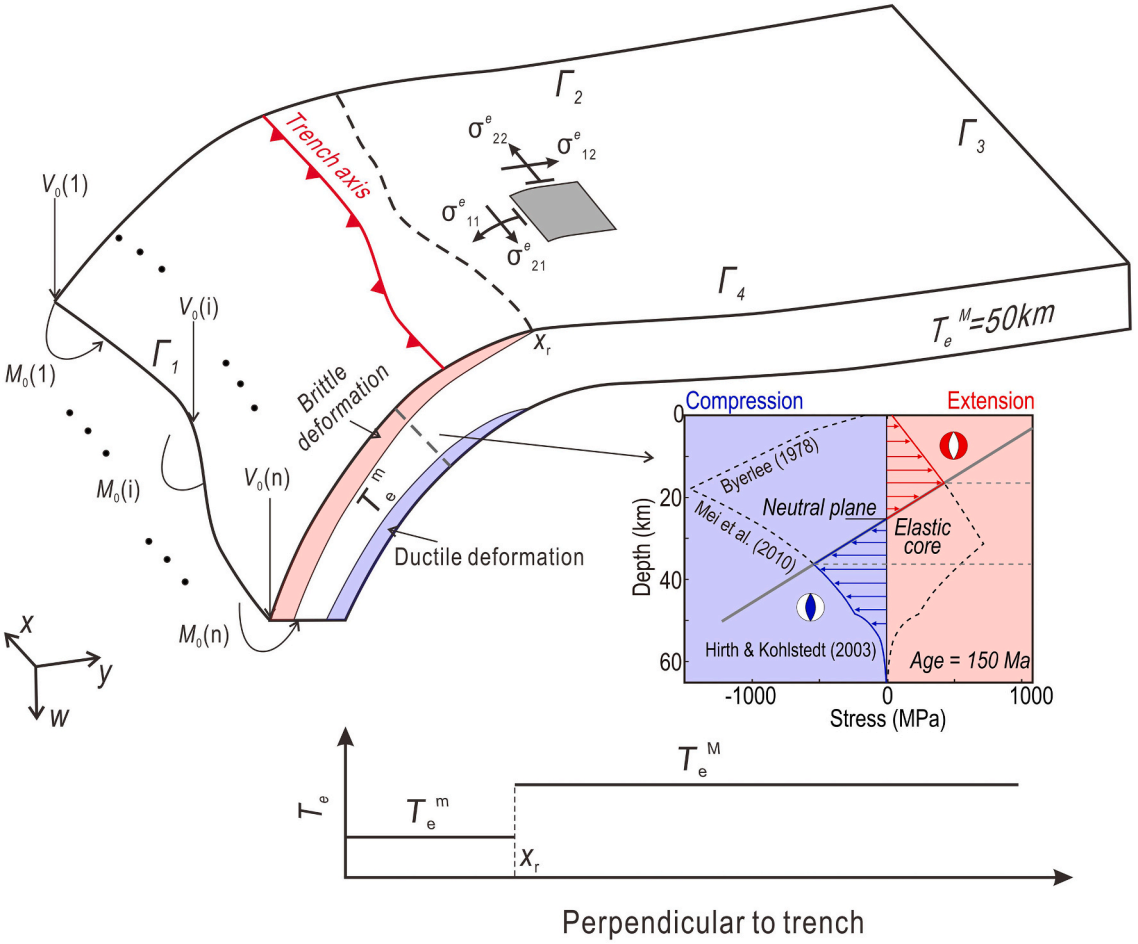

Fig. 3. Schematic 3-D model used in our study. Γ_1 - Γ_4 represent different boundary conditions (Please see eq. 4). The M_0 and V_0 change along the strike of trench. For simplicity, the T_e was divided into two parts (T_e^M and T_e^m). The T_e^M is set to a constant (50 km) in our model (Following the work of Zhang et al., 2014) while T_e^m vary freely along the strike of the trench. Intra-plate extensional earthquakes usually occurred in the brittle deformation domain and the compressional earthquakes usually occurred in the ductile deformation domain.

previous studies (Contreras-Reyes and Osses, 2010). The T_e^M represents the ambient T_e where the curvature of plate is zero (Contreras-Reyes and Osses, 2010) and the T_e^m stands for landward T_e deduced by normal faults. The relationship between T_e and oceanic plate age is controversial. Some studies suggest no correlation (Bry and White, 2007; Cary and Copley, 2014), or a weak correlation between the two (Contreras-Reyes and Osses, 2010); while others indicate a strong relationship (Hunter and Watts, 2016; Zhang et al., 2018a). At the southern Mariana subduction zone, however, the calculated T_e^M in different studies are close, ~58 km (Hunter and Watts, 2016) and ~ 50 km (Zhang et al., 2014, 2018a). We thus set the T_e^M as a constant (50 km) while allow the T_e^m to vary freely along the trench (Fig. 3).

In order to avoid the effects of seamounts and plateau close to the subduction zone, the calculated area is set to a rectangle with x axis perpendicular to the trench and y axis along the trench (Fig. 3). Compared with the 3-D model of Zhang et al. (2019) which used trench axis as subducting model boundary, the subducting boundary (north) of our model is ~100 km landward of the trench (the thick red rectangle in Fig. 1). The best fit model was constrained by bathymetry seaward of trench axis and plate interface of the Slab 2.0 (Hayes, 2018) landward of the trench axis. The part shallower than 60 km in Slab 2.0 was taken as the constraint. The effects of deeper slab (beyond the red rectangle in

Table 1
Parameters used in flexural analysis.

Model	Symbol	Description	Value	Unit
Flexural model (Formula 1)	E	Young's modulus	7×10^{10}	Pa
	g	Acceleration due to gravity	9.81	m/s^2
	ν	Poisson's ratio	0.25	
	ρ_m	Mantle density	3300	kg/m^3
	ρ_c	Crust density	2700	kg/m^3
	ρ_s	Sediment density	2000	kg/m^3
	ρ_w	Water density	1030	kg/m^3
PSO inversion (Formula 3)	c_1	Individual learning rate	2	
	c_2	Social parameter	2	
	r_1	Tuning parameter 1	Random in (0, 1)	
	r_2	Tuning parameter 2	Random in (0,1)	
	ω	inertia weight	From 0.9 to 0.2	

Fig. 1) were considered as boundary loadings (such as M_0 and V_0) in our model. This setting can help to keep the outer rise area away from the boundary, so the boundary effect can be neglected. It also helps us better to handle the effect due to local topographic reliefs such as seamounts. Since our aim is to model the first-order deformation of the subducting plate, the local topographic reliefs are noise and thus need to be removed in our simulation.

2.3. Inversion strategy

In previous 2-D inversion works, there are commonly three (Levitt and Sandwell, 1995) or five (Contreras-Reyes and Osses, 2010) variables to be inverted. It is straightforward to invert these parameters by minimizing the w_{rms} between model result and the observation with the calculated model: $W_{RMS} = \sqrt{\frac{1}{N}\sum_{i=1}^{N}\left(w_i^{obs} - w_i^{cal}\right)^2}$, where N is the number of points along the profiles, w^{obs} is the observation (bathymetry or gravity anomaly) and w^{cal} is the calculated result (Bry and White, 2007; Contreras-Reyes and Osses, 2010; Zhang et al., 2014; Hunter and Watts, 2016). However in the 3-D case, the M_0 and V_0 are vectors rather than single values, and T_{e} becomes a two-dimensional matrix. In our study, $T_{\mathrm{e}}^{\mathrm{M}}$ and x_{r} are set to be 50 km and 200 km, respectively. There are three groups of parameters $\{M_0, V_0, T_{\mathrm{e}}^{\mathrm{m}}\}$ to be inverted. The number of parameters depends on the nodes of the model. For example, the node number of model is 200 × 200, the elements number of M_0 is 200 theoretically. Here, we used the control point method (CPM) to carry out the inversion for brevity in which only a few control points are assigned values in each parameter of $\{M_0, V_0, T_{\mathrm{e}}^{\mathrm{m}}\}$ and the values of other nodes are given by interpolation. In this study we set 7 control points, the total number of parameters is 21. Parameters are searched by particle swam optimization (*PSO* method) (Shi and Eberhart, 1998).

The PSO method is a group based optimization technology which treat the optimization as the process of birds flying and looking for food. In the solution space, every solution was considered as a particle (bird) and the "good or bad" (or the fitness) of each particle can be determined by the *RMS* error function, the smaller of *RMS* the better of the particle. Particles are not independent of each other and they can adjust their velocities and positions by learning the experience of themselves and others.

Suppose there are n particles in an M-dimension searching space. At t moment (namely the tth iterations), the position of ith particle in solution space is $X_i^t = (x_{i1}^t, x_{i2}{}^t, x_{i3}{}^t, \ldots, x_{iM}{}^t)$, and the velocity of the particle is $V_i{}^t = (v_{i1}{}^t, v_{i2}{}^t, v_{i3}{}^t, \ldots, v_{iM}{}^t)$, where $i = 1, 2, 3, \ldots, n$. The position and velocity of the particle at next moment $(t + 1)$ are given by:

$$\begin{aligned} V_i^{t+1} &= \omega V_i^t + c_1 r_1 (P_i^t - X_i^t) + c_2 r_2 \left(P_{gm}{}^t - X_i^t\right) \\ X_i^{t+1} &= X_i^t + V_i^{t+1} \\ i &= 1, 2, 3, \ldots, n \end{aligned} \tag{3}$$

where $P_{\mathrm{i}}^t = (p_{i1}^t, p_{i2}{}^t, p_{i3}{}^t, \ldots, p_{iM}{}^t)$ is the best position (fitness) of the i th particle in the whole history (from the first iteration to the present). $P_{gm}^t = (p_{g1}^t, p_{g2}{}^t, p_{g3}{}^t, \ldots, p_{gM}{}^t)$ is the best position (fitness) of any of the particles in the whole history. c_1 and c_2 represent learning factors which are non-negative constants. c_1 reflects the influence from itself and c_2 reflects the influence from the society. In general, $(c_1 + c_2)$ should be no >4 (Shi and Eberhart, 1998). r_1 and r_2 are independent random numbers distributing uniformly in (0,1). Inertia weight ω is also a non-negative number, reflecting the influence of previous velocity on current velocity. If ω is large, the global search ability of particles is strong. Otherwise, the local search ability of particles is strong. In general, ω is set to be within (0.1, 1). Please note that the initial X_{i}^0 and V_i^0 are given randomly (Shi and Eberhart, 1998). In our inversion, both c_1 and c_2 equal to 2 and ω changes from 0.9 to 0.2. These parameters are empirical values and would affect the convergence rate of inversion but not the results (Zhang et al., 2019). The validity and details of inversion method have been described in Zhang et al. (2019). Our aim is to find a best fitting of combination of $X_0 = \{M_0, V_0, T_{\mathrm{e}}^{\mathrm{m}}\}$ to minimize the *RMS* error function and each X_0 is a particle in the *PSO* inversion.

Compared with 2-D models, our 3-D model shows smoother results due that 2-D models fail to consider the effect from the dimension along the strike of trenches. The difference of parameter inversion between 2-D and 3-D model can reach ~30% when plate bending changes along the trench strike (Zhang et al., 2018b). However the change trend of 2-D and 3-D model is consistent. So we used previous 2-D model results (Zhang et al., 2014) to help us to constrain the solution space, giving the range for M_0, V_0 and T_{e}. Then, we adjusted the solution space through the *PSO* inversion method (Fig. 4) and finally we obtained the best one.

2.4. Plane stress distribution

In a thin elastic plate model, the plate bending stress changes linearly with depth (z), where z represents the distance from the neutral plane. The stress is tensional above the neutral plane and becomes compressive at greater depths. Therefore, the plane stress calculated at any depth including the plate surface, can be used to infer the stress level at other depths because of the linear dependence.

The components of the plane stress along the direction normal (x) and parallel (y) to the trench are given by (Zhang et al., 2022):

$$\begin{bmatrix} \sigma_{11} \\ \sigma_{22} \\ \sigma_{12} \end{bmatrix} = -\frac{Ez}{1+\nu} \begin{bmatrix} \frac{1}{1-\nu} & \frac{\nu}{1-\nu} & 0 \\ \frac{\nu}{1-\nu} & \frac{1}{1-\nu} & 0 \\ 0 & 0 & 1 \end{bmatrix} \begin{bmatrix} \frac{\partial^2 w}{\partial x^2} \\ \frac{\partial^2 w}{\partial y^2} \\ \frac{\partial^2 w}{\partial x \partial y} \end{bmatrix} \tag{4}$$

where E and ν represent the Young's modulus and the Poisson's ratio, which are set to 7×10^{10} Pa and 0.25, respectively (Table 1). According to the work of Contreras-Reyes and Osses (2010), The Young's modulus can be described by: $E = \rho V_p(1 + \nu^2)$, in which V_p is P-wave velocity and ρ is density. Serpentinization of mantle at outer rise can result in decrease of V_p and ρ and increase of ν (Contreras-Reyes and Osses, 2010). Therefore the lateral variation of E may have influence on stresses along the bending direction but nearly no influence along the strike of trench. When we discuss the elastic core and the depth of plastic deformation constrained by the YSE, these stress components are projected onto the principal stress axes by:

$$\begin{aligned} \sigma_1 &= \frac{\sigma_{11} + \sigma_{22}}{2} + \sqrt{\left(\frac{\sigma_{11} - \sigma_{22}}{2}\right)^2 + \sigma_{12}{}^2} \\ \sigma_2 &= \frac{\sigma_{11} + \sigma_{22}}{2} - \sqrt{\left(\frac{\sigma_{11} - \sigma_{22}}{2}\right)^2 + \sigma_{12}{}^2} \end{aligned} \tag{5}$$

3. Results

3.1. Statistics of fault strike and seismicity at outer rise

We have identified ~260 bending-related faults from the multibeam bathymetry data using the same method with Ranero et al. (2005) (Figs. 2a and b). The rose diagram shows that the main direction of the fault strike is ENE and thus the bending direction is NNW (Fig. 2b). Outer rise earthquakes are concentrated in the east of the Challenger Deep (~220–260 km), exhibiting an evidently non-uniform distribution in the along-trench histogram (within a distance of 200 km perpendicular to the trench) (Fig. 2c). Nearly 25% of these earthquakes occur at depths shallower than 6 km and ~ 75% of earthquakes are located shallower than 50 km (Fig. 2d). Although focal mechanisms of most earthquakes in Zhu et al. (2019) are unknown, moment tensor solutions from the GCMT catalog exhibit strike-slip and normal faulting mechanisms, indicating that some old, less-ideally oriented faults may be reactivated.

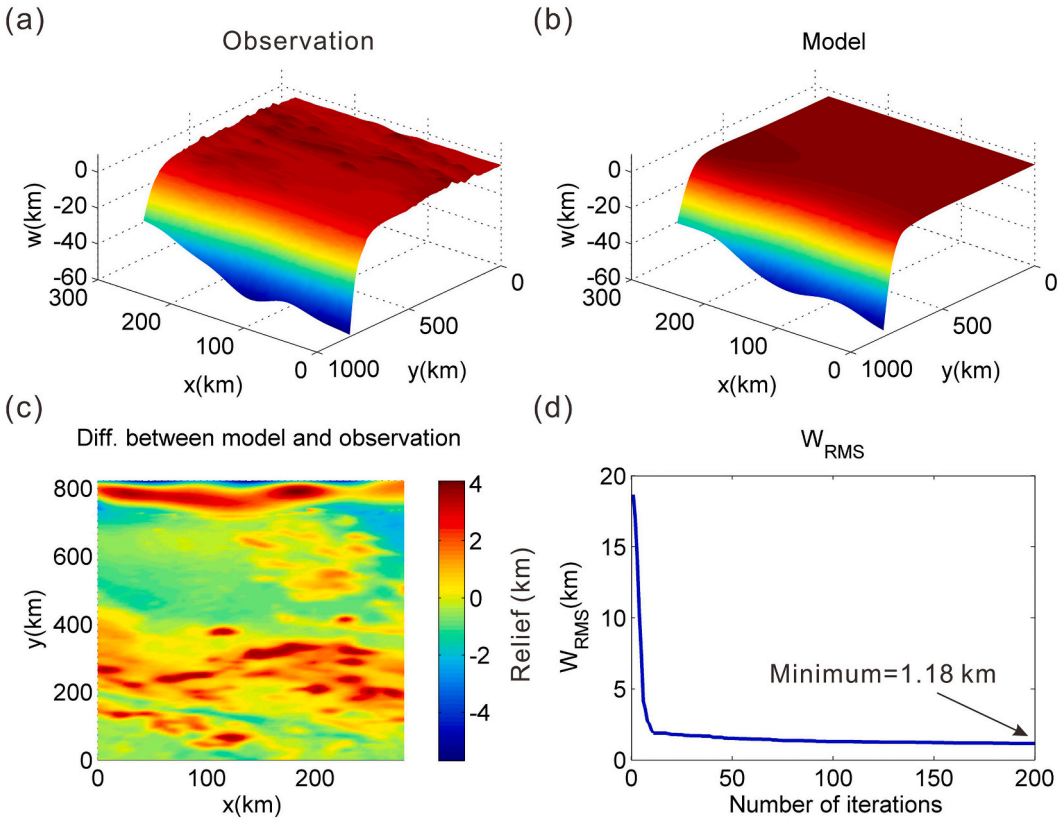

Fig. 4. Final model of the *PSO* inversion. (a) The observation of bathymetry (Tozer et al., 2019) and slab 2.0 data (Hayes, 2018). (b) Result of our model. (c) The difference between our mode and the observation. (d) RMS error function changes with the number of iterations. The boundary depth of model is close to that of observation overall.

3.2. Plate bending

A series of inversions have been performed for a large range of M_0, V_0, and T_e and our best-fit model has a W_{rms} <1.2, yielding smooth model results (Figs. 4 and 5b). We compare the results with data along two different profiles perpendicular to trench, one profile along the trench (Fig. 5f), and another one along the base of slab in our model. In both trench-normal profiles (Fig. 5c and d) and the one along the base of the slab (Fig. 5e), the modeled deformation matches very well with the data (Fig. 5c and d). However, the fit between model and data gets slightly worse along the trench. Although the overall trench shape matches reasonably well, the model results do not completely capture the small-wavelength variation and underestimate the trench depth at certain places, including the Challenger Deep (Fig. 5e).

To match the plate deformation, both plate bending moment and vertical loadings (M_0 and V_0) are applied on the plate boundary with along-strike variation. The V_0 applied on the western part (near the Challenger Deep) is nearly twice as much as that of the eastern part (Fig. 5f). The M_0 changes from positive to negative in a narrow range (~100–170 km) and the T_e^m changes from ~16 to 40 km at the southern Mariana (Fig. 3f).

3.3. Distribution of plane stresses

According to eqs. (1) and (2), the distribution of plane stress components σ_{11}^e, σ_{22}^e, σ_{12}^e (Fig. 3), and the maximum principal stress σ_1^e are calculated in the best-fit model (Fig. 6). σ_{11}^e stands for the normal stress along the direction perpendicular to the trench that is caused by plate bending and reaches maximum close to the trench axis. σ_{22}^e represents the normal stress along trench that reflects the trench-parallel flexural deformation of the plate. σ_{12}^e represents shear stress on the *x*-*y* plane, which also corresponded to lateral flexural deformation. If no lateral change in plate pulling exists, the σ_{12}^e is zero.

We find that the stress distribution associated with plate bending is heterogeneous (Fig. 6). In addition, σ_{11}^e increases gradually from the outer rise to the trench and reaches the maximum at the Challenger Deep (Fig. 6a), consistent with previous studies (Zhang et al., 2014, 2019). The difference between our work and previous 2-D works is that our model shows a smoother result because 2-D model failed to reflect the real 3-D deformation. σ_{22}^e varies along the trench and reaches the maximum at ~143°E, 11–11.5°N, corresponding to the place where M_0 and V_0 change sharply (Figs. 5f and 4b). The value of σ_{12}^e changes from positive to negative from east to west along the trench (Fig. 6c). Among the three stress components, σ_{11}^e is the largest, reaching the maximum of ~5 GPa. Consequently, the maximum value of σ_1^e exceeds 6 GPa (Fig. 6d).

4. Discussion

4.1. Flexural parameters vary along the trench

Along the strike of southern Mariana trench axis, both trench axis depth and slab depth increase from east to west, suggesting a good consistent between deep slab deformation and shallow plate bending (Fig. 5e). The exception is the area between ~100 km and ~ 180 km on the profile (Fig. 5e), where the trench axis depth is shallow while the slab depth is deep. Both the M_0 and the V_0 also change sharply here (Fig. 5f). It may be caused by the variation of the slab length along the trench axis. Zhu et al. (2019) showed that the length of slab shortened significantly near the Challenger Deep and thus may influence the depth of trench axis. Another possible reason is that local terrain, such as seamounts or plateau, results in a relatively shallow trench depth. The

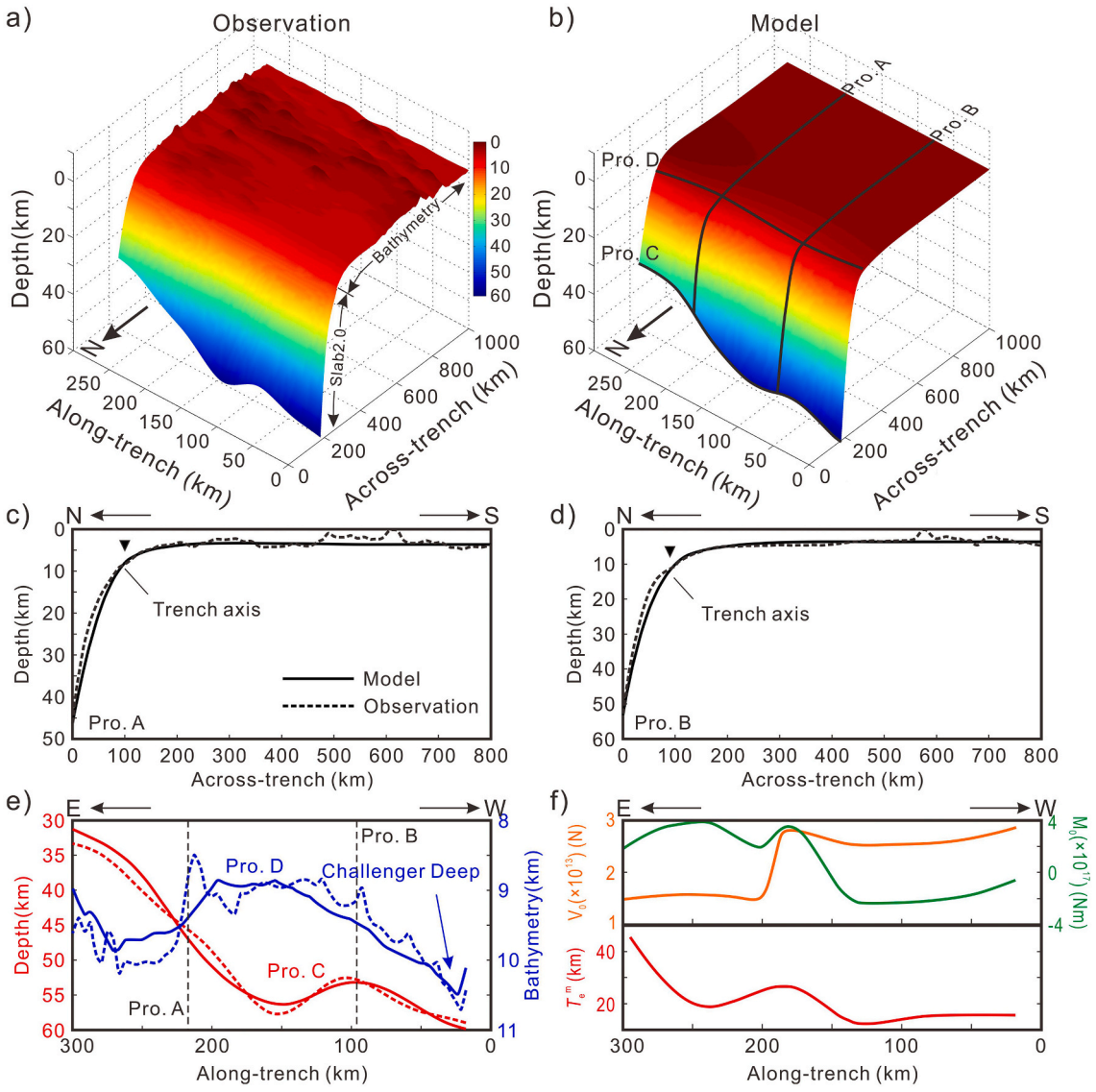

Fig. 5. Result of our model. (a) Observed plate bending of the study area. The observation comes from the combination of the global 15 arc-second resolution bathymetry data (Tozer et al., 2019) and the Slab 2.0 data (Hayes et al., 2018). (b) 3-D flexural model results. Pro. A, B, C, and D represent the profiles shown in Fig. 5c-e. The Pro. D is along the trench axis. (c) - (e) Comparisons between our model and observed data along different profiles in Fig. 5(b). The dashed lines represent the observation and the solid lines are results of our model. (f) The variation of inverted M_0 (blue line) and V_0 (orange line) along the plate boundary. (For interpretation of the references to colour in this figure legend, the reader is referred to the web version of this article.)

T_e^m decreases as it approaches the Challenger Deep (Fig. 5f), suggesting that the degree of plate weakening becomes larger from west (near the Guam) to east (near the Challenger Deep) (Contreras-Reyes and Osses, 2010). This is due to the fact that the plate deflection reaches maximum at the Challenger Deep and generates a lot of normal faults, which bring more sea water into the crust and upper mantle resulting in the plate hydration, possibly leading to further plate weakening.

4.2. Comparison between 2-D and 3-D models on estimating the bending stress

Garcia et al. (2019) suggested that the amount of strain ε (as well as the stress σ) of a flexural plate can be described by:$\varepsilon = -z\frac{\partial^2 w}{\partial x'^2}$, where z is the distance from the neutral plane and x' is the horizontal coordinate axis along the direction of maximum curvature. The bending stress is given by: $\sigma = -\frac{E}{1-u^2}\varepsilon$. It shows that if the z is a constant (e.g. at the upper surface of the plate), the amplitude of bending stress relies only on the bend curvature of plate. However, it's difficult to identify in 2D whether a selected profile is along the direction of maximum curvature even the profile is perpendicular to the trench. In 3D models, we calculate the magnitude and direction of maximum curvature by projecting the directions of arbitrary orthogonal curvature to the directions of the maximum and minimum curvature (Zhang et al., 2021). If M_0 and V_0 are invariant along trench, the direction of maximum curvature is perpendicular to the trench and the bending stress estimated by the 2-D model is nearly equal to that estimated by the 3-D model. Otherwise, the direction of maximum curvature will change and point to the lowest place in a three-dimensional space. In this situation, the bending stress estimated by the 2-D profile curvature may be underestimated.

We built a test model to illustrate how along-strike variable V_0 leads to an underestimate of 2-D bending stress (Fig. 7). In the test model, V_0 changes from V_0^1 to V_0^2 linearly within a distance L along strike, and the T_e is set to a constant value (35 km) (Fig. 7a). We carry out 21 different

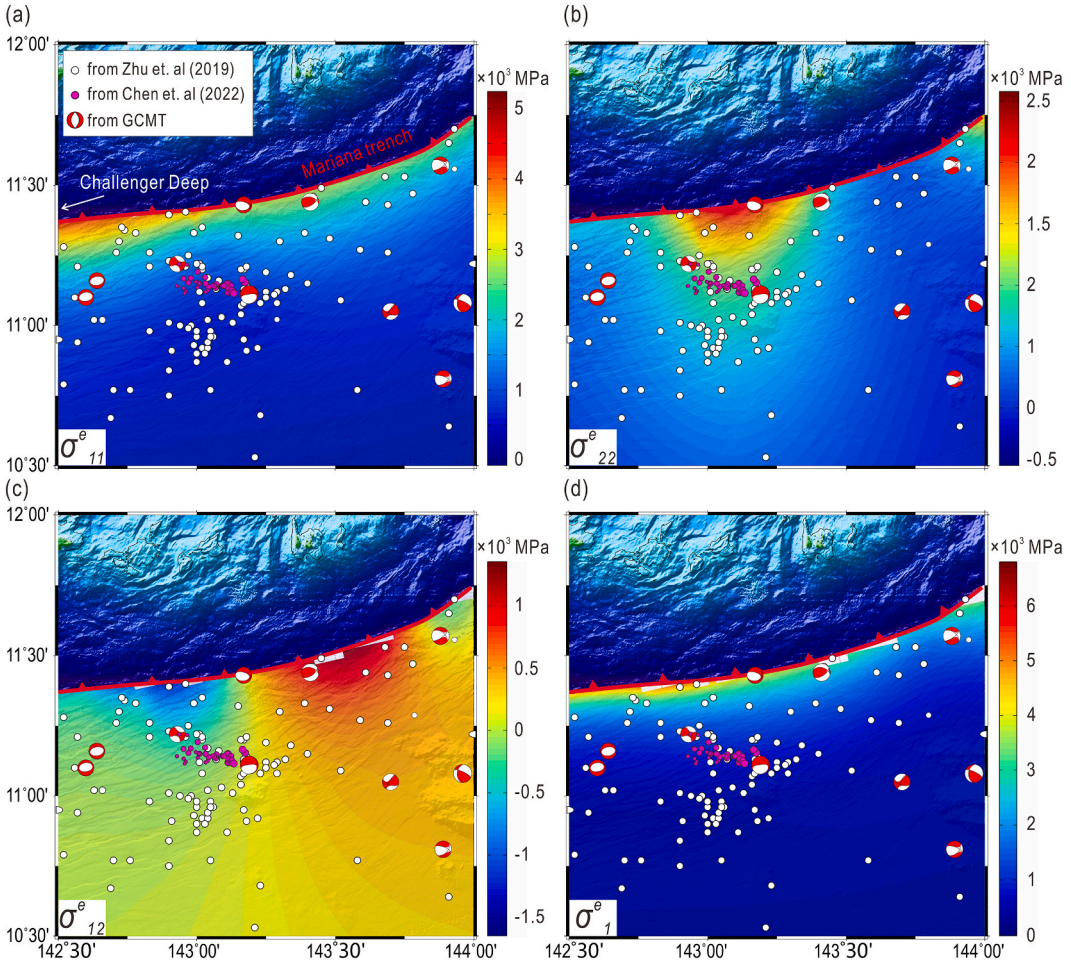

Fig. 6. The components of the bending stress. The white circles represent the location of outer rise earthquakes proposed by Zhu et al. (2019) and the magenta circles are outer rise earthquakes from Chen et al. (2022). Variable radiuses of circles represent the event magnitudes. Focal mechanism solutions come from GCMT. (a) The distribution of σ^e_{11}, the normal stress along the direction perpendicular to the trench. The yellow star stands for the location of the Challenger Deep. (b) The distribution of σ^e_{22}, the normal stress along the strike of the trench, and (c) The distribution of the plane shear stress σ^e_{12}. (d) The distribution of the maximum principal stress σ^e_1 (Please see the eq. (2)). (For interpretation of the references to colour in this figure legend, the reader is referred to the web version of this article.)

calculation models in which the ratio V_0^2/V_0^1 and L/L_m are set to different values (every red dot in Fig. 7d represents one model). We then find that the changes in both V_0 and the variation distance L (we used L/L_m in Fig. 7d, where L_m is the width of our model) can affect the results, in which the bending stress increases with V_0 and decreases with L (Fig. 7d). Considering the Mariana Trench, if the L/L_m equals to 0.1 and V_0^2/V_0^1 is set to 2, the difference between 2-D and 3-D models can exceed 20% (Fig. 7).

4.3. Trench-parallel of plane stress and outer rise earthquakes

Non-uniformly distributed outer rise earthquakes have been observed along various subduction zones (Ranero et al., 2005; Ammon et al., 2008; Lay et al., 2018). For example at the northeastern Alaska subduction zone, the USGS National Earthquake Information Center (NEIC) catalog shows that most of outer rise events larger than magnitude 4.5 since 1900 were distributed near the Kodiak Island (Lay et al., 2018). Here we show the variation in bending deformation and plane stress of the outer rise region. Such trench-parallel variation in plane stress may be a mechanism for the non-uniform distribution of outer rise earthquakes. In the southern Mariana Trench, the along-trench variations of σ^e_{22} and σ^e_{12} are more dominant than σ^e_{11} (Fig. 6). The location of the drastic changes in σ^e_{22} and σ^e_{12} coincides with an earthquake cluster in the outer rise of Mariana (Zhu et al., 2019) (Fig. 6b and c), indicating a possible relationship. Such along-trench variation in stress distribution may be correlated with outer rise earthquake distribution in other subduction zones (Sandiford et al., 2020; Ye et al., 2021; Craig et al., 2022). We believe that greater bending stress may increase the possibility of outer rise seismicity.

In addition to normal faulting earthquakes, strike-slip earthquakes have been reported at the outer rise of subduction zones, such as the 1940 Mw 7.3 Mariana earthquake (Okal et al., 2013), as well as some strike-slip outer rise earthquakes with Mw 5–7 at southern Mariana subduction zone (Emry et al., 2014). Lay et al. (2018) suggested that the strike-slip events in outer rise required laterally varying plate boundary conditions, such as the ~52 mm/yr of transform motion along the Queen Charlotte Fault along the eastern boundary in in the Gulf of Alaska (Brothers et al., 2020). Besides, Chen et al. (2022) located ~2000 earthquakes using the machine-learning-based earthquake detection method and depicted a normal fault by an outer-rise sub-cluster. This normal fault penetrated to a depth of 50 km and may be cause by the reactivation of the inherited fabrics (Chen et al., 2022). Here, we propose a possible mechanism that the laterally varying plate deflection can generate heterogeneous stress distribution in the outer rise region, resulting in unevenly distributed outer rise earthquakes and reactivation of remnant fabric. Preexisting weak faults, such as abyssal hill faults, may be reactivated and may exhibit strike-slip faulting mechanism due to such stress heterogeneity (Fig. 8). If plate deflection does not change along trench, bending stress would be uniform along the trench. It will more likely generate new trench-parallel normal faults instead of

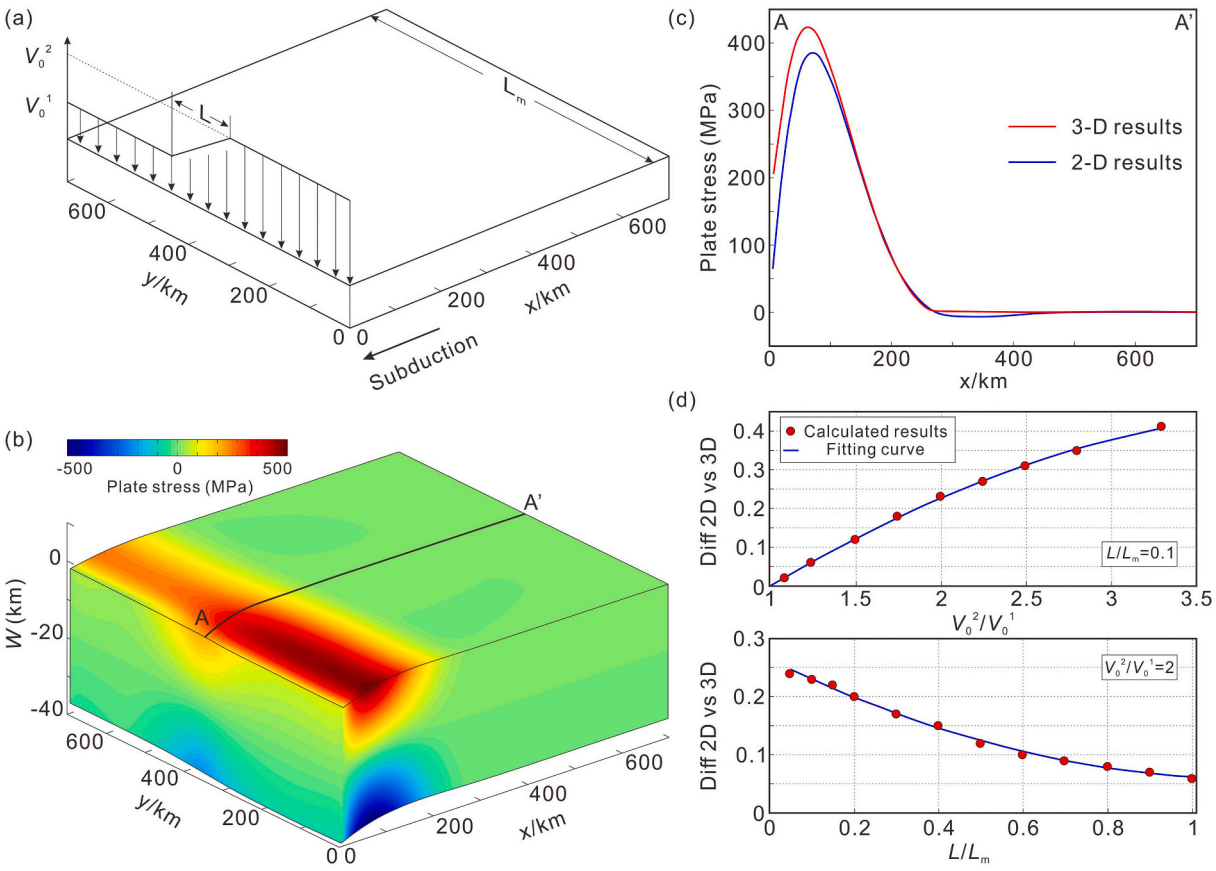

Fig. 7. The difference between the 2-D and the 3-D model on estimating the bending stress. (a) Schematic 3-D model to illustrate the along-strike variable V_0. L is the variation distance of V_0 and L_m is the width of our model. (b) The 3-D bending stress distribution under the loading shown in Figure a. The difference of the bending stress between the 2-D and the 3-D model along the profile A-A' in Figure b. (d) Plotting difference between the 2-D and the 3-D model on estimating bending stress versus the change of V_0 (V_0^2/V_0^1) and the L/L_m.

reactivating preexisting weak faults, when preexisting faults have a angle (> 25°) oblique to the trench axis (Red and blue arrows in Fig. 8) (Billen et al., 2007). Otherwise, it may cause the change of the direction of the maximum extensional bending stress in the variable zone which may provide greater possibilities for reactivation of preexisting weak faults (Green arrows in Fig. 8). When the direction of the maximum bending stress differs from the strike of preexisting weak faults, it may cause strike-slip movement on the fault. In addition, extensional strain in the red square area is larger than that in the green square area, suggesting a higher likelihood of fault activation in the red square region (Fig. 8).

4.4. Reasons causing variation of plate bending stress and outer rise seismicity

Previous studies showed that regional stress caused by the resistance of overriding plate played an important role in the distribution of outer rise seismicity by changing the plate bending stress (Ward, 1984; Christensen and Ruff, 1988; Ammon et al., 2008). Some other works suggested that seamount subduction could influence the seismicity (Kodaira et al., 2000; Mochizuki et al., 2008; Wang and Bilek, 2014). However in our study area, there is only a small seamount close to the trench and the locations of this cluster of earthquakes seem to have no clear relation with the seamount.

Our simulations show that the change of plate deflection along the strike of the trench may be another reason to cause variation of bending stress and outer rise seismicity. Through analysis of the well-located seismicity using near-field OBS data, Zhu et al. (2019) found that length and dip angle of the subducting slab increased from SW to NE along the trench. We infer that the variation of plate bending deformation may result from the combination of slab pull and interface resistance.

5. Conclusion

By analyzing the results of plate bending deflection, plane stress, and the distribution of outer rise earthquakes at the southern Mariana Trench, the following conclusions are obtained:

(1) The variable boundary loadings along the strike of southern Mariana Trench can cause not only along-strike variation in plate deflection, but also in plane stresses. The boundary loading applied at the Challenger Deep area is nearly twice as much as that of other areas. Under this situation, the difference on estimating the bending stress exceeds 20% between 2-D and 3-D models by considering curvature of the trench.
(2) The plane maximum curvature of the plate reflects the stress distribution of bending plate and well matches the outer rise earthquake cluster in the southern Mariana subduction zone, suggesting that the variation of plane stress may influence the distribution of extensional earthquakes in outer rise.
(3) We propose a 3-D flexural model, considering the along-strike variable plate deflection and its influence on plane deformation. It shows that lateral plate deflection can cause the change of the direction of the maximum extensional bending stress which may result in reactivation of preexisting weak faults, providing a

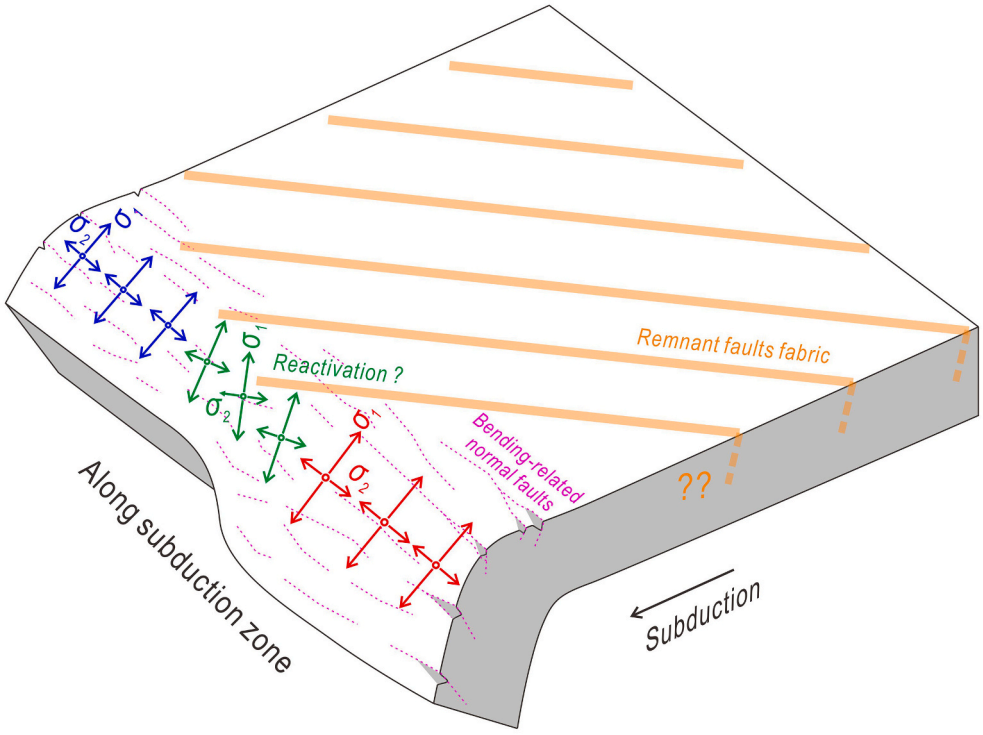

Fig. 8. Conceptual map of how the along-strike variable plate deflection influences the plane deformation of bending plate. It shows that if plate deflection does not change along trench, bending stress would be uniform along the trench. It will more likely generate new trench-parallel normal faults (Red and blue arrows). Otherwise, it may cause the change of the direction of the maximum extensional bending stress and provide greater possibilities for reactivation of preexisting weak faults (Green arrows). (For interpretation of the references to colour in this figure legend, the reader is referred to the web version of this article.)

possible mechanism to generate the outer rise strike-slip earthquakes.

CRediT authorship contribution statement

Jiangyang Zhang: Conceptualization, Methodology, Software, Investigation, Writing – original draft. **Hongfeng Yang:** Conceptualization, Writing – original draft, Supervision, Project administration, Data curation, Investigation, Visualization. **Gaohua Zhu:** Data curation, Investigation, Visualization. **Han Chen:** Data curation, Investigation, Visualization. **Fan Zhang:** Investigation, Visualization, Project administration. **Zhen Sun:** Investigation, Visualization, Project administration.

Declaration of Competing Interest

The authors declare that they have no known competing financial interests or personal relationships that could have appeared to influence the work reported in this paper.

Data availability

The data are available online (https://figshare.com/articles/dataset/S_Mariana/12841676). The bathymetry data can be found at the website: https://gamone.whoi.edu/thredds/catalog/usgs/data0/bathy/srtm15_plus/catalog.html?dataset=usgs/data0/bathy/srtm15_plus/topo15.grd. The multibeam data with ~150 m resolution can be found at the NOAA website: https://www.ngdc.noaa.gov/maps/autogrid/ and the global slabs geometry data Slab 2.0 can be found at https://www.sciencebase.gov/catalog/item/5aa1b00ee4b0b1c392e86467 (Hayes et al., 2018).

Acknowledgements

We are grateful to Prof. Jian Lin, Dr. Xiaohuan Jiang, Xiang Chen, Suli Yao, Pengcheng Zhou and Junhao Song for useful discussion. We thank Zhongxian Zhao and Zhiyuan Zhou for offering technical assistance. GMT (Wessel and Smith, 1995) was used to draw the topographic map.

This research is supported by the National Natural Science Foundation of China (No. 92158205, 42206071, 41976064, 92258303), Guangdong NSF research team project (2017A030312002), Hong Kong Research Grant Council Grants (No. 14304820, 14306119), Laoshan Laboratory project (LSKJ202204100), Faculty of Science at CUHK, China Postdoctoral Science Foundation (No. 2019M663119).

References

Ammon, C.J., Kanamori, H., Lay, T., 2008. A great earthquake doublet and seismic stress transfer cycle in the central Kuril islands. Nature 451, 561–566.
Beavan, J., Wang, X., Holden, C., Wilson, K., Power, W., Prasetya, G., Bevis, M., Kautoke, R., 2010. Near-simultaneous great earthquakes at Tongan megathrust and outer rise in September 2009. Nature 466, 959–963.
Bilham, R., Bendick, R., Wallace, K., 2003. Flexure of the Indian Plate and intraplate earthquakes. J. Earth Syst. Sci. 112 (3), 315–329.
Billen, M., Cowgill, E., Buer, E., 2007. Determination of fault friction from reactivation of abyssal-hill faults in subduction zones. Geology. 35 (9), 819–822.
Brothers, D.S., Miller, N.C., Barrie, J.V., Haeussler, P.J., Greene, H.G., Andrews, B.D., et al., 2020. Plate boundary localization, slip-rates and rupture segmentation of the Queen Charlotte Fault based on submarine tectonic geomorphology. Earth Planet. Sci. Lett. 530, 115882 https://doi.org/10.1016/j.epsl.2019.115882.
Bry, M., White, N., 2007. Reappraising elastic thickness variation at oceanic trenches. J. Geophys. Res. 112 https://doi.org/10.1029/2005JB004190.
Cary, T.J, Copley, A., 2014. An explanation for the age independence of oceanic elastic thickness estimates from flexural profiles at subduction zones, and implications for continental rheology. Earth Planet. Sci. Lett. 392, 207–216.
Chapple, W.M., Forsyth, D.W., 1979. Earthquakes and bending of plates at trenches. J. Geophys. Res. 84 (B12), 6729–6749.
Chen, H., Yang, H., Zhu, G., Xu, M., Lin, J., You, Q., 2022. Deep outer-rise faults in the Southern Mariana Subduction Zone indicated by a machine-learning-based high-resolution earthquake catalog. Geophys. Res. Lett. 49, e2022GL097779.
Christensen, D.H., Ruff, L.J., 1983. Outer rise earthquakes and seismic coupling. Geophys. Res. Lett. 10, 697–700.
Christensen, D.H., Ruff, L.J., 1988. Seismic coupling and outer rise earthquakes. J. Geophys. Res. 93 (B11), 13,421-13,444.
Contreras-Reyes, E., Osses, A., 2010. Lithospheric flexure modelling seaward of the Chile trench: implications for oceanic plate weakening in the Trench Outer rise region. Geophys. J. Int. 182 (1), 97–112.

Craig, T.J., Methley, P., Sandiford, D., 2022. Imbalanced moment release within subducting plates during initial bending and unbending. J. Geophys. Res. Solid Earth 127, e2021JB023658. https://doi.org/10.1029/2021JB023658.
Duputel, Z., Kanamori, H., Tsai, V.C., Rivera, L., Meng, L., Ampuero, J.-P., Stock, J.M., 2012. The 2012 Sumatra great earthquake sequence. Earth Planet. Sci. Lett. 351-352, 247–257. https://doi.org/10.1016/j.epsl.2012.07.017.
Emry, E.L., Wiens, D.A., Garcia-Castellanos, 2014. Faulting within the Pacific plate at the Mariana Trench: Implications for plate interface coupling and subduction of hydrous minerals. J. Geophys. Res. Solid Earth 119, 2076–3095.
Garcia, E.S., Sandwell, D.T., Bassett, D., 2019. Outer Trench Slope Flexure and Faulting at Pacific Basin Subduction zones. Geophys. J. Int. https://doi.org/10.31223/osf.io/dbn8j.
Grevemeyer, I., Kaul, N., Diaz-Naveas, J.L., Villinger, H., Ranero, C.R., Reichert, C., 2005. Heat flow and bending-related faulting at subduction trenches: Case studies offshore of Nicaragua and Central Chile. Earth Planet. Sci. Lett. 236, 238–248.
Gusman, A.R., Tanioka, Y., Matsumoto, H., Iwasaki, S.-I., 2009. Analysis of the Tsunami Generated by the Great 1977 Sumba Earthquake that Occurred in Indonesia. Bull. Seismol. Soc. Am. 99 (4), 2169–2179.
Hayes, G., 2018. Slab2 - A Comprehensive Subduction Zone Geometry Model: U.S. Geological Survey Data Release. https://doi.org/10.5066/F7PV6JNV.
Hunter, J., Watts, A.B., 2016. Gravity anomalies, flexure and mantle rheology seaward of circum-Pacific trenches. Geophys. J. Int. 207 (1), 288–316.
Kodaira, S., Takahashi, N., Nakanishi, A., Miura, S., Kaneda, Y., 2000. Subducted Seamount Imaged in the Rupture Zone of the 1946 Nankaido Earthquake. Science. 289, 104–106.
Lay, T., Ammon, C.J., Kanamori, H., Rivera, L., Koper, K.D., Hutko, A.R., 2010. The 2009 Samoa-Tonga great earthquake triggered doublet. Nature 466, 964–967.
Lay, T., Ye, L., Bai, Y., Cheung, K.F., Kanamori, H., 2018. The 2018 M_W 7.9 Gulf of Alaska Earthquake: Multiple Fault Rupture in the Pacific Plate. Geophys. Res. Lett. 45, 9542–9551.
Levitt, D.A., Sandwell, D.T., 1995. Lithospheric bending at subduction zones based on depth soundings and satellite gravity. J. Geophys. Res. 100, 379–400.
Lynnes, C., Lay, T., 1988. Source process of the great Sumba earthquake. J. Geophys. Res. 93, 13,407-14,320.
Manríquez, P., Contreras-Reyes, E., Osses, A., 2014. Lithospheric 3-D flexure modelling of the oceanic plate seaward of the trench using variable elastic thickness. Geophys. J. Int. 196, 681–693.
Masson, D.G., 1991. Fault patterns at outer trench walls. Mar. Geophys. Res. 13 (3), 209–225. https://doi.org/10.1007/bf00369150.
Mochizuki, K., Yamada, T., Shinohara, M., Yamanaka, Y., Kanazawa, T., 2008. Weak interplate coupling by seamounts and repeating M similar to 7 earthquakes. Science 321 (5893), 1194–1197.
Mortera-Gutiérrez, C.A., Scholl, D.W., Carlson, R.L., 2003. Fault trends on the seaward slope of the Aleutian Trench: implications for a laterally changing stress field tied to a westward increase in oblique convergence. J. Geophys. Res. 108, 2477.
Okal, E.A., Reymond, D., Hongsresawat, S., 2013. Large, pre-digital earthquakes of the Bonin-Mariana subduction zone, 1930–1974. Tectonophysics. 586, 1–14.
Pegler, G., Das, S., 1996. The 1987-1992 Gulf of Alaska earthquakes. Tectonophysics 257, 111–136.
Ranero, C.R., Morgan, J.P., McIntosh, K., Reichert, C., 2003. Bending-related faulting and mantle serpentinization at the Middle America trench. Nature 425 (6956), 367–373.
Ranero, C.R., Villaseñor, A., Morgan, J.P., Weinrebe, W., 2005. Relationship between bending-faulting at trenches and intermediate-depth seismicity. Geochem. Geophys. Geosyst. 6 (12).
Sandiford, D., Moresi, L.M., Sandiford, M., Farrington, R., Yang, T., 2020. The fingerprints of flexure in slab seismicity. Tectonics 39. https://doi.org/10.1029/2019TC005894 e2019TC005894.
Scholz, C.H., Campos, J., 1995. On the mechanism of seismic decoupling and back arc spreading at subduction zones. J. Geophys. Res. 100 (B11), 22,103–22,115.
Shi, Y.H., Eberhart, R.C., 1998. A modified particle swarm optimizer. Proc. IEEE Int. Conf. Evol. Comp. 69–73.
Timoshenko, S., Woinowsky-Krieger, S., 1959. Theory of Plates and Shells, 2nd edition. McGraw-Hill Press, New York, p. 591.
Tozer, B., Sandwell, D.T., Smith, W.H.F., Olson, C., Beale, J.R., Wessel, P., 2019. Global Bathymetry and Topography at 15 Arc Seconds: SRTM15+. Sci. Lett, Earth planet. https://doi.org/10.1029/2019ea000658.
Turcotte, D., Schubert, G., 2014. Geodynamics, 3nd edn. Cambridge University Press, p. 626.
Wang, K., Bilek, S.L., 2014. Invited review paper: Fault creep caused by subduction of rough seafloor relief. Tectonophysics. 610, 1–24.
Ward, S.N., 1984. A note on lithospheric bending calculations. Geophys. J. R. Astron. Soc. 78, 241–253.
Watts, A.B., 2001. Isostasy and Flexure of the Lithosphere, 1st edn. Cambridge University Press, New York, p. 478.
Wessel, P., Smith, W.H.F., 1995. New version of the Generic Mapping Tools released. Eos. Transactions American Geophysical Union 76 (33), 329.
Ye, L., Lay, T., Kanamori, H., 2021. The 25 March 2020 M W 7.5 Paramushir, northern Kuril Islands earthquake and major ($M_W \geq 7.0$) near-trench intraplate compressional faulting. Earth Planet. Sci. Lett. 556, 116728.
Yoshida, Y., Satake, K., Abe, K., 1992. The large normal-faulting Mariana earthquake of April 5, 1990 in uncoupled subduction zone. Geophys. Res. Lett. 19 (3), 297–300.
Zhang, F., Lin, J., Zhan, W., 2014. Variations in oceanic plate bending along the Mariana trench. Earth Planet. Sci. Lett. 401, 206–214.
Zhang, F., Lin, J., Zhou, Z., Yang, H., Zhan, W., 2018a. Intra- and intertrench variations in flexural bending of the Manila, Mariana and global trenches: implications on plate weakening in controlling trench dynamics. Geophys. J. Int. 212, 1429–1449.
Zhang, J., Sun, Z., Xu, M., Yang, H., Zhang, Y., Li, F., 2018b. Lithospheric 3-D flexural modelling of subducted oceanic plate with variable effective elastic thickness along the Manila Trench. Geophys. J. Int. 215, 2071–2092.
Zhang, J., Sun, Z., Qiu, N., Zhang, Y., Li, F., 2019. 3-D effective elastic thickness inversion of subduction zone based on particle swarm optimization algorithm. Chinese J. Geophys. (in Chinese) 62 (12), 4738–4749.
Zhang, J., Zhang, F., Lin, J., Yang, H., 2021. Yield failure of the subducting plate at the Mariana Trench. Tectonophysics. 814, 228944.
Zhang, J., Sun, Z., Yang, H., Zhang, F., 2022. A model of plate bending at the transition zone from subduction to collision in northernmost Manila trench. Geophys. Res. Lett. 49 https://doi.org/10.1029/2022GL100474 e2022GL100474.
Zhou, Z., Lin, J., 2018. Elasto-plastic deformation and plate weakening due to normal faulting in the subducting plate along the Mariana Trench. Tectonophysics 734, 59–68.
Zhou, Z., Lin, J., Behn, M.D., Olive, J.A., 2015. Mechanism for normal faulting in the subducting plate at the Mariana Trench. Geophys. Res. Lett. 42, 4309–4317.
Zhu, G., Yang, H., Lin, J., Zhou, Z., Xu, M., Sun, J., Wan, K., 2019. Along-strike variation in slab geometry at the southern Mariana subduction zone revealed by seismicity through ocean bottom seismic experiments. Geophys. J. Int. 218 (3), 2122–2135.
Zhu, G., Wiens, D.A., Yang, H., Lin, J., Xu, M., You, Q., 2021. Upper mantle hydration indicated by decreased shear velocity near the Southern Mariana Trench from Rayleigh wave tomography. Geophys. Res. Lett. https://doi.org/10.1029/2021GL093309.